EDGE ARTICLE

Check for updates

All publication charges for this article have been paid for by the Royal Society of Chemistry

Symmetry-breaking charge separation in perylene diimide trimers: effects of aggregation and solvent polarity

Lie Tian,†[a] Guangliu Ran, [iD] †*[ab] Shixuan Zheng[c] and Wenkai Zhang [iD] *[ab]

Symmetry-breaking charge separation (SB-CS) is a fundamental process in natural photosynthetic systems, serving as the primary trigger for electron transfer and ultimately leading to the formation of a charge separated state. This mechanism has also been leveraged in optoelectronic devices to minimize energy loss and improve solar energy conversion efficiency. However, in organic solar cell (OSC) studies, SB-CS has predominantly been observed in polar environments, and the roles of molecular aggregation in modulating this process remain unclear. Herein, we investigated the influence of aggregation and solvent polarity on the SB-CS of the perylene diimide trimer (PDI-III) in different solvents. Steady-state absorption and fluorescence spectroscopy reveal that PDI-III exhibits a biphasic aggregation behavior depending on solvent polarity, with stronger aggregation occurring in both nonpolar and highly polar solvents than in solvents of intermediate polarity. Femtosecond transient absorption spectroscopy and time-resolved infrared spectroscopy indicate that SB-CS also emerges in toluene, with an extent that lies between those observed in chloroform and acetone. Further analysis suggests that in toluene, intermolecular aggregation strengthens $\pi-\pi$ interactions and electronic coupling, thereby enabling SB-CS even in the absence of substantial solvent polarity. In acetone, intramolecular aggregation, together with strong solvent polarity, leads to more efficient SB-CS than in chloroform. Collectively, these results establish a clear mechanistic framework for how aggregation and solvent polarity govern SB-CS in PDI-III, offering guiding principles for minimizing energy loss while maintaining high photocurrent in next-generation OSCs.

Introduction

Significant advances in nonfullerene acceptor (NFA)-based organic solar cells (OSCs) have enabled power conversion efficiency (PCE) exceeding 20%.[1–5] However, their PCEs still lag behind those of perovskite or crystalline silicon solar cells, primarily due to large energy loss.[6–8] Owing to the intrinsically low permittivity of OSCs, the previously prevailing view held that a driving force of ∼0.3 eV in fullerene-based OSCs was required to dissociate charge transfer (CT) excitons into free charge carriers (FCs), thereby contributing substantially to the overall energy loss.[9,10] This driving force can be approximated by the lowest unoccupied molecular orbital (LUMO) energy offset between the donor and acceptor for electron transfer, or by the highest occupied molecular orbital (HOMO) energy offset for hole transfer.[11] Interestingly, recent studies have demonstrated that small, or even negative energy offset can achieve high PCE with relatively low energy loss in NFA-based systems.[12–14] Although multiple factors have been proposed to influence this behavior, a consensus on the underlying mechanism has yet to be reached.[15–18] In this context, symmetry-breaking charge separation (SB-CS) has emerged as a particularly compelling pathway, as it can facilitate more efficient FCs generation due to its lower charge separation barrier compared to conventional excitons.[19–21]

Perylene diimide (PDI) is one of the most extensively investigated NFAs, owing to its strong light-harvesting capability, tunable absorption characteristics, high chemical and thermal robustness, and excellent electron-accepting properties.[22–24] State-of-the-art devices often employ architectures that integrate multiple PDI subunits into twisted frameworks. Such molecular designs promote long-range molecular ordering, enhance optical absorption, and mitigate energy loss associated with charge recombination and excimer formation.[25–27] Importantly, these structural features not only govern the ground state optical responses of PDI assemblies but also shape their excited state landscape, within which SB-CS may emerge.[28–30] For

[a]School of Physics and Astronomy, Applied Optics Beijing Area Major Laboratory, Center for Advanced Quantum Studies, Beijing Normal University, Beijing 100875, China. E-mail: wkzhang@bnu.edu.cn; bnurgg@bnu.edu.cn

[b]Key Laboratory of Multiscale Spin Physics, Ministry of Education, Beijing Normal University, Beijing 100875, China

[c]Beijing National Laboratory for Molecular Science, State Key Laboratory of Rare Earth Materials Chemistry and Applications, College of Chemistry and Molecular Engineering, Peking University, Beijing 100871, China

† These authors contributed equally to this work.

example, Guo *et al.* synthesized two PDI dimers with different conjugated bridge structures and found that SB-CS occurs only in polar solvents, whereas it is absent in weakly polar and nonpolar environments.[31] Lin *et al.* further investigated covalently linked slip-stacked PDI dimers and trimers, revealing that vibronic coupling can mediate excited-state mixing between excitonic and CT configurations, and that the trimer architecture offers an intrinsic advantage for SB-CS by enabling richer exciton/CT-state mixing beyond the dimer limit.[32] Nevertheless, most previous studies have focused on polar solvents, where solvent fluctuation is essential for breaking the excited state symmetry. In contrast, SB-CS in nonpolar media remains largely unexplored, despite the fact that the active layers of OSCs typically operate in nonpolar environments.[33] This makes understanding SB-CS under nonpolar conditions particularly important.

In this work, we investigate the SB-CS behavior of a PDI trimer (PDI-III), in which three monomer (PDI-C5) units are covalently linked to a central benzene core *via* acetylene bridges. The solvent-dependent aggregation of PDI-III was investigated using UV-Vis absorption and fluorescence spectroscopy, while femtosecond transient absorption spectroscopy (TAS) and time-resolved infrared (TRIR) spectroscopy were employed to probe its excited state dynamics. Analysis of the UV-Vis absorption and fluorescence spectra reveals that PDI-III exhibits a biphasic aggregation behavior depending on the solvent polarity, with stronger aggregation observed in both nonpolar and highly polar solvents compared to solvents of intermediate polarity. TAS and TRIR further demonstrate that SB-CS occurs not only in polar solvents but also in nonpolar solvents, with the extent of charge separation in nonpolar solvent toluene (TOL) lying between that observed in moderately polar solvent chloroform (CF) and highly polar solvent acetone (AC). These findings highlight that both aggregation and solvent polarity synergistically modulate SB-CS in PDI-III, providing mechanistic insights for strategies aimed at reducing energy loss in OSCs.

Results and discussion

The molecular structure of PDI-III is shown in Fig. 1a, and the reference monomer PDI-C5 is presented in Fig. S1. PDI-III is a C_3-symmetrical star-shaped molecule composed of three PDI-C5 units, each of which is connected to the central phenyl group *via* an acetylene bridge.[34] The rotational flexibility of the alkyne bonds and the confined space around the trimer chromophore allow the solvent to modulate both intramolecular and intermolecular interactions, potentially affecting the aggregation behavior and excited state dynamics of PDI-III. The UV-Vis spectra of PDI-C5 and PDI-III in various solvents are shown in Fig. S2. PDI-C5 exhibits four characteristic absorption peaks at approximately 530 (A_{0-0}), 490 (A_{0-1}), 460 (A_{0-2}), and 425 (A_{0-3}) nm, with decreasing intensity. These peaks correspond to the aromatic core $\pi-\pi^*$ transition in the series of vibronic relaxation of the S_0-S_1 states (Fig. S2a).[35] With increasing solvent polarity, the absorption peaks of PDI-C5 exhibit only minor red or blue shifts without changes in the relative intensities, indicating that PDI-C5 remains largely monomeric in solution.[36] In contrast, PDI-III (Fig. S2b) exhibits pronounced spectral variations as the solvent polarity increases. In both nonpolar and polar solvents, the spectra display an inversion in intensity between A_{0-0} and A_{0-1}, characteristic of molecular aggregation.[37] Conversely, in solvents of intermediate polarity, the spectral profiles closely resemble those of the monomer. These results indicate that PDI-III exhibits a biphasic aggregation behavior in solution.[38] Based on this, three representative solvents with distinct polarities—TOL, CF, and AC—were selected to investigate this behavior in detail.

The normalized UV-Vis absorption and fluorescence spectra of PDI-III in three representative solvents are shown in Fig. 1b. In the intermediate polarity solvent CF, the absorption spectrum exhibits four vibronic bands at 542 (A_{0-0}), 505 (A_{0-1}), 472 (A_{0-2}), and 446 nm (A_{0-3}) with decreasing intensity, closely resembling those of the PDI-C5 monomer (Fig. S2a). The fluorescence spectrum in CF is nearly a mirror image of the absorption, consistent with typical monomeric behavior.[39] In contrast, in nonpolar solvent TOL, the UV-Vis spectrum of PDI-III exhibits an inversion of the A_{0-0} and A_{0-1} band intensities
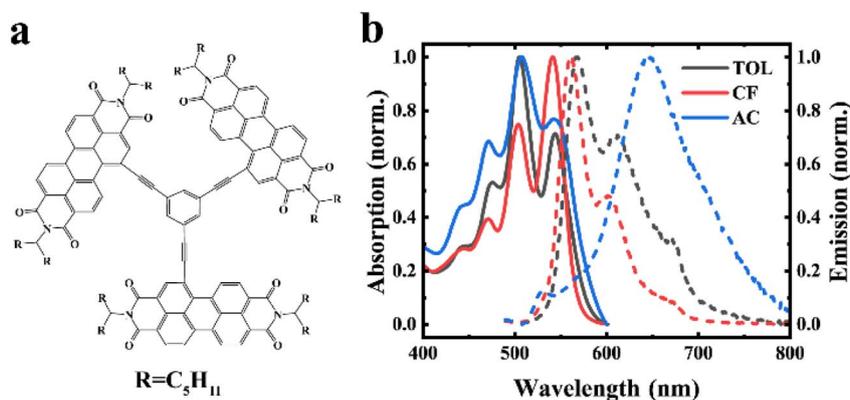

Fig. 1 (a) The molecular structure of PDI-III. (b) Normalized UV-Vis absorption (solid line) and fluorescence (dashed line) spectra of PDI-III in three representative solvents. All fluorescence spectra were recorded upon excitation at 480 nm.

and broadened vibronic features compared to CF. The corresponding fluorescence is also broader, reflecting aggregation-induced excitonic interactions.[40] In AC, a similar A_{0-0} and A_{0-1} intensity inversion is observed, but the fluorescence is further broadened, less structured, and red-shifted to around 650 nm, indicating the emergence of polar-solvent-assisted symmetry-breaking.[41,42]

Concentration-dependent absorption spectroscopy was employed to distinguish intramolecular and intermolecular aggregation of PDI-III,[43] with the results shown in Fig. S3. In TOL (Fig. S3a), the degree of aggregation decreases with decreasing concentration, consistent with intermolecular aggregation. By contrast, in AC (Fig. S3c), the aggregation exhibits only slight variation with changing concentration, indicative of intramolecular aggregation.[43] In CF, PDI-III remains monomeric across all concentrations (Fig. S3b). To gain deeper insight into the aggregation behavior, comprehensive conformational searches were carried out for PDI-III and its dimer using Molclus,[44] followed by Gibbs free energy calculations (see the Computational methods section in the SI for details). The Gibbs free energy difference is defined as $\Delta G = G_{dimer} - 2G_{monomer}$. In acetone, the calculated ΔG value for the dimer is +7.2 kcal mol^{-1} (Table S1), indicating that the monomer is thermodynamically more stable. The lowest-energy monomer structure obtained from the conformational search exhibits pronounced intramolecular aggregation characteristics, in which two PDI units are coupled in a single trimer (Fig. S4a). In contrast, in toluene, the calculated ΔG value for the dimer is −6.8 kcal mol^{-1} (Table S1), demonstrating that dimer formation is thermodynamically favored (Fig. S4b). This behavior is likely associated with the ability of aromatic solvents to π-stack with the PDI cores.[45,46] The π–π interactions between toluene molecules and the PDI framework may induce a more extended molecular conformation, thereby weakening intramolecular aggregation and promoting intermolecular π–π stacking between adjacent PDI-III units. As a result, dimer formation is energetically preferred in toluene. To further characterize the excited states, we measured the fluorescence lifetimes of PDI-III in the three solvents and determined the corresponding fluorescence quantum yields. The results are summarized in Table 1, and the corresponding decay curves are shown in Fig. S5. Notably, PDI-III exhibits the highest fluorescence quantum yield in CF, while it is significantly reduced in both TOL and AC. These results indicate that in TOL and AC, a larger portion of the excited state population relaxes non-radiatively, while a smaller fraction returns to the ground

state *via* radiative decay. The slightly longer fluorescence lifetime of PDI-III in TOL relative to CF, combined with the lower fluorescence quantum yield, suggests that aggregation-induced symmetry breaking may stabilize a charge separated state,[18,47] as further corroborated by subsequent TAS and TRIR measurements. In AC, a longer lifetime component emerges, consistent with the formation of charge separation state through polar-solvent-assisted symmetry-breaking.[31]

To further investigate the excited state dynamics of PDI-III in different solvents, TAS measurements were carried out with 480 nm excitation, and the results are presented in Fig. 2. For comparison, the corresponding TAS spectra of the reference monomer PDI-C5 are shown in Fig. S6. In TOL (Fig. 2a–c), where PDI-III tends to aggregate, two negative bands of comparable intensity are observed between 490 and 570 nm. By comparison with the UV-Vis absorption and fluorescence spectra, the former can be assigned to ground-state bleaching (GSB), while the latter arises from a superposition of GSB and stimulated emission (SE). Upon increasing the delay time from 0.2 to 75 ps (Fig. 2a), two new excited state absorption (ESA) bands emerge at 598 and 803 nm, accompanied by two isosbestic points at approximately 710 and 850 nm, which are absent in the monomer reference (Fig. S6a). According to previous reports, these ESA bands can be attributed to PDI radical cation and anion species, providing unambiguous evidence for the formation of the SB-CS state in TOL.[29] The spectral signals persist throughout the experimental time window (3.6 ns), indicating a long-lived charge recombination (CR) process following the SB-CS state (Fig. 2c).

When PDI-III is dissolved in CF (Fig. 2d and e), three negative features appeared immediately after photoexcitation. The negative signal around 510 nm is assigned to GSB, while the SE band appears around 610 nm, consistent with the fluorescence spectrum. The sharp, high-intensity signal at 540–580 nm belongs to the superposition signal of GSB and SE. This pronounced mountain-like negative profile resembles that of the PDI-C5 monomer (Fig. S6b); however, the ESA features differ significantly. The ESA band at 735 nm that synchronizes with GSB belongs to the locally excited (LE) state.[41] The broad positive feature around 800 nm, which is absent in the monomer spectra, is attributed to overlapping absorption from the PDI anion and CT state.[41] The signal of the PDI radical cation is not observed over the entire time window, likely because the strong SE in CF, arising from its high fluorescence quantum yield, obscures the relatively weak cation absorption. These observations indicate that only weak charge separation occurs *via* SB-CS in CF. In AC (Fig. 2g and h), two negative bands appear immediately after photoexcitation. The spectral profile differs from that of the PDI-C5 monomer in AC (Fig. S6c), consistent with the previous discussion that PDI-III undergoes intramolecular aggregation. Fig. 2g exhibits two well-defined positive bands at 619 and 700 nm, which are assigned to the PDI radical cation and LE state, respectively, while the absorption band around 800 nm is attributed to overlap between the PDI anion and CT state. The presence of a distinct radical cation and anion bands, together with the low fluorescence quantum yield, indicates that SB-CS is more pronounced in AC than in CF. To

Table 1 Refractive index (n), dielectric constant (ε), fluorescence quantum yield (Φ) and fluorescence lifetime (τ_f) of PDI-III in selected solvents

Solvent	n	ε	$f(\varepsilon) - f(n^2)^a$	Φ	τ_f (ns)
Toluene	1.50	2.38	0.03	0.40	5.85
Chloroform	1.45	4.81	0.30	0.68	5.59
Acetone	1.36	20.7	0.57	0.16	8.21, 27.70

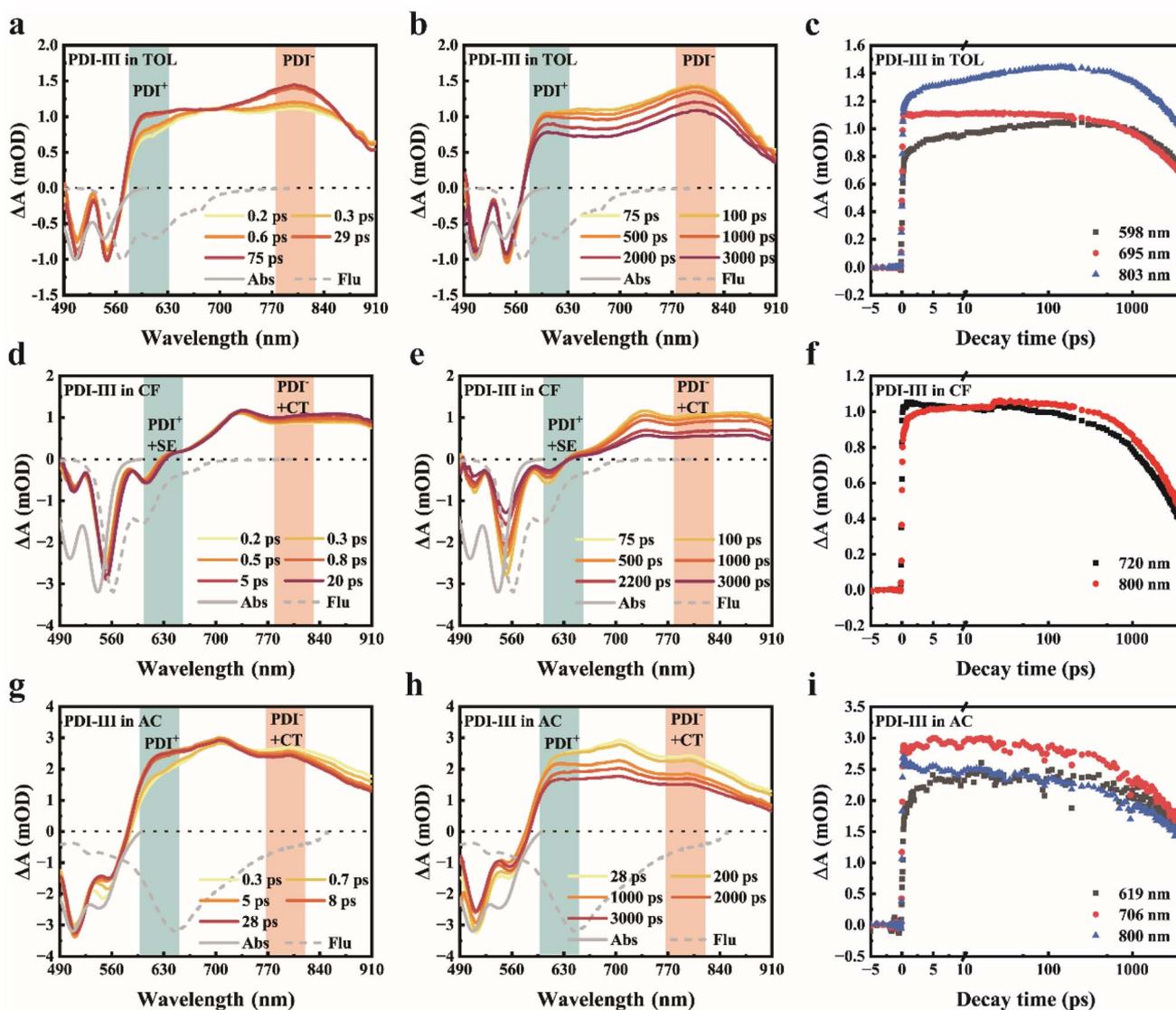^{a} $f(x) = 2(x − 1)/(2x + 1)$: Onsager functions.

Fig. 2 TAS spectra of PDI-III in (a–c) toluene, (d–f) chloroform, and (g–i) acetone, recorded at short (a, d and g) and long (b, e and h) time delays following 480 nm excitation. The solid and dashed gray lines represent the UV–Vis absorption and fluorescence spectra, respectively. Panels (c, f and i) present the kinetic traces at selected wavelengths.

exclude nonlinear contributions that may be enhanced in aggregated samples, we performed pump-fluence-dependent TAS measurements. The normalized kinetic traces overlap across all pump fluences used in this work (Fig. S7), indicating that the formation and decay dynamics are independent of excitation density within the investigated range and thus ruling out significant higher-order or bimolecular contributions under our experimental conditions.

Based on the above spectroscopic analysis, a simplified energy-level scheme is proposed to rationalize the solvent-dependent excited state dynamics of PDI-III (Fig. 3). Upon photoexcitation, the LE state is generated and rapidly relaxes to the CT state. The CT state can either decay to the ground state or undergo symmetry breaking to form the SB-CS state. The SB-CS state may return to the CT manifold *via* back electron transfer or recombine directly to the ground state.[41,48] To quantify the excited state decay dynamics of PDI-III in different solvents,

global target analysis was performed using the kinetic model illustrated in Fig. 3. The resulting species-associated difference spectra (SADS) and corresponding time-dependent concentration kinetics are presented in Fig. 4, with the extracted time constants for the relevant excited state processes summarized in Table 2. The experimental data and corresponding global fitting results are shown in Fig. S8, demonstrating the excellent agreement between the experiment and the model.

The first component obtained from global fitting is assigned to the LE state, which decays fastest in AC (0.93 ps), followed by TOL (1.05 ps) and CF (1.30 ps). The second component corresponds to the CT state, with decay time constants to the ground state nearly identical to the fluorescence lifetimes (Table 1). The third component represents the SB-CS state, for which the charge separation process occurs fastest in AC (330 ps), followed by TOL (420 ps) and CF (690 ps), indicating that SB-CS efficiency is highest in AC, intermediate in TOL, and lowest in CF.
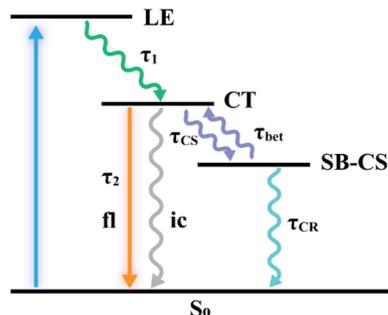
Fig. 3 Simplified energy diagram illustrating the solvent-dependent excited state dynamics of PDI-III in different solvents. τ_1 denotes the time constant associated with the formation of the relaxed CT state; τ_2 corresponds to the decay of the CT state back to the ground state; τ_{CS} represents the charge-separation time constant; τ_{bet} is the time constant for back electron transfer; and τ_{CR} describes the charge-recombination process.

Table 2 Time constants of PDI-III in different solvents obtained from global fitting of TAS data

Solvent	τ_1 (ps)	τ_2 (ns)	τ_{CS} (ps)	τ_{bet} (ns)	τ_{CR} (ns)
Toluene	1.05 ± 0.04	5.3 ± 0.5	420 ± 30	5.7 ± 0.4	14 ± 1
Chloroform	1.30 ± 0.01	5.2 ± 0.4	690 ± 30	5.4 ± 0.5	7.8 ± 0.8
Acetone	0.93 ± 0.01	9 ± 2	330 ± 10	8.3 ± 0.6	19 ± 2

Although TAS provides an overview of the excited state dynamics, the significant spectral overlap among GSB, SE, and ESA signals from different species complicates the identification of the SB-CS related features. To overcome this limitation, we further performed TRIR measurements, in which the C≡C stretching vibration serves as a spectrally isolated and highly sensitive probe of electronic redistribution.[49] This feature enables direct and unambiguous tracking of the SB-CS process.

For a symmetric molecular structure, the electronic distributions across the C≡C linkers are uniform, resulting in a single C≡C stretching band. Upon symmetry breaking, the uneven electron distribution gives rise to distinct C≡C stretching frequencies for different linkers. When symmetry is fully broken and the electrons are completely localized on a specific branch, a single C≡C band reappears.[50] Fig. 5 presents the TRIR spectra in the C≡C stretching region following 480 nm excitation of PDI-III in different solvents, with the corresponding Fourier transform infrared spectrometer (FTIR) spectra shown in Fig. S9. Upon photoexcitation, a broad, featureless positive band emerges in the mid-IR region. Similar bands have been previously assigned to the $S_2 \leftarrow S_1$ transition.[51] In our case, this structureless background exhibits significant growth at early times in TOL and CF (Fig. 5a and b) and persists well beyond 2000 cm^{-1} (Fig. S10), which is inconsistent with $S_2 \leftarrow S_1$ transitions and thus excludes this possibility. We instead attribute this band to the absorption of FCs, as commonly observed in inorganic semiconductor photocatalysts and organic photovoltaics.[52,53]

As shown in Fig. 5b, in CF, a single positive peak around 2115 cm^{-1} appears immediately after excitation, followed by the
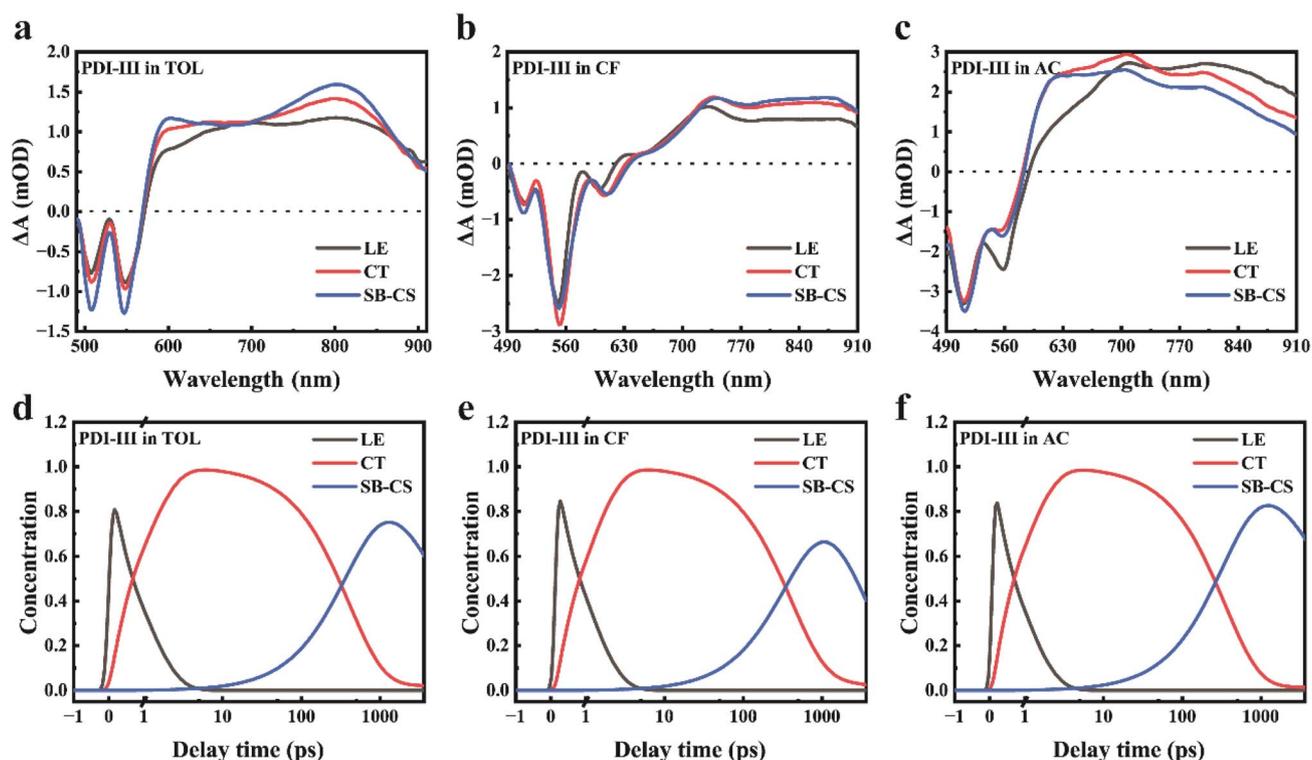

Fig. 4 Global target analysis results derived from TAS of PDI-III. SADSs and temporal concentrations of PDI-III in (a and d) toluene, (b and e) chloroform, and (c and f) acetone.
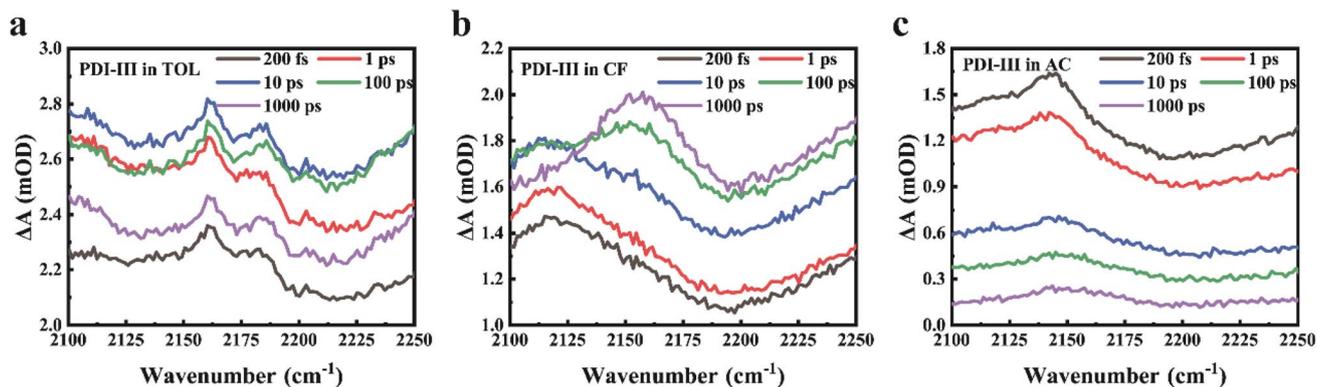
Fig. 5 TRIR spectra of PDI-III in the C≡C stretching region in toluene (a), chloroform (b), and acetone (c) following 480 nm excitation.

emergence of a second peak around 2152 cm^{-1} at later times. In contrast, in AC, two ESA peaks at 2112 and 2150 cm^{-1} appear rapidly after excitation, with the lower-frequency band decaying quickly and leaving only the 2150 cm^{-1} peak at later times. These observations indicate that symmetry breaking is more pronounced in AC than in CF, in agreement with the TAS results. The enhanced symmetry breaking in AC primarily arises from its higher polarity and intramolecular aggregation, which together stabilize the charge-separated state. In TOL, two positive ESA peaks at 2161 cm^{-1} and 2185 cm^{-1} persist throughout the measurement window, indicating that SB-CS can also occur in this nonpolar solvent. As discussed above, PDI-III in TOL tends to undergo intermolecular aggregation, which may arise from the ability of aromatic solvents to π-stack with the PDI cores.[45,46] This aggregation strengthens π–π interactions and increases electronic coupling between neighboring PDI units. The enhanced coupling renders the excited state more prone to electronic asymmetry, promoting the concentration of the electron on a specific branch.[54,55] As a result, aggregation effectively promotes SB-CS. Importantly, the distinct vibrational frequencies observed in different aggregation environments suggest that the excited-state energy landscape is strongly modulated by aggregation geometry. Variations in electronic coupling alter the degree of charge delocalization and the stabilization energy of the symmetry-broken state, which is directly reflected in the solvent-dependent shifts of the ESA bands. To further examine whether the observed SB-CS is retained in a more device-relevant environment, we extended our investigation from solution to the solid state. In neat PDI-III films (Fig. S11), the TAS spectra exhibit broad positive photo-induced absorption together with an isosbestic point, suggesting that charge separation persists even under the low-dielectric conditions of the solid state. We next coupled PDI-III with the electron donor material, PBDB-T, to examine whether charge separation is preserved under donor–acceptor conditions. In the PBDB-T:PDI-III blend film (Fig. S12), a pronounced growth of the PBDB-T GSB is observed at later delay times. The temporal evolution of the donor bleach provides strong evidence that charge separation is retained under donor–acceptor solid-state conditions.

Conclusions

In summary, we synthesized a PDI trimer and investigated its aggregation behavior and excited state dynamics in solution. Steady-state absorption and fluorescence spectroscopy revealed that the trimer exhibits biphasic aggregation, with stronger aggregation observed in both nonpolar and highly polar solvents compared to solvents of intermediate polarity. Based on these observations, three representative solvents were selected for further study. Analysis of the fluorescence quantum yields indicates that in nonpolar TOL and highly polar AC, a larger portion of the excited state population relaxes to a non-radiative state, while a smaller fraction returns to the ground state radiatively, compared to intermediate polarity CF. TAS and TRIR measurements reveal that SB-CS occurs in all three solvents, with the extent of charge separation in TOL intermediate between that observed in CF and AC. In TOL, intermolecular aggregation enhances π–π interactions and electronic coupling between PDI units, promoting SB-CS even in the absence of a polar environment. In AC, rapid electron localization on a specific branch and an accelerated charge separation process are observed, reflecting the combined effect of intramolecular aggregation and solvent polarity in promoting SB-CS. In contrast, only weak SB-CS is detected in CF, attributable to its modest solvent polarity. Collectively, these results establish that both aggregation and solvent polarity critically govern SB-CS, with aggregation serving as a key driving force even under nonpolar conditions. These insights provide a mechanistic basis for controlling SB-CS to reduce energy loss while sustaining high photocurrent in next-generation OSCs.

Author contributions

Guangliu Ran and Wenkai Zhang: conceptualization and supervision; Lie Tian, Guangliu Ran, and Shixuan Zheng: measurements and data analysis; Lie Tian and Guangliu Ran: investigation and writing the original draft; Guangliu Ran and Wenkai Zhang: review and editing.

Conflicts of interest

There are no conflicts to declare.

Data availability

The data supporting this study are available within the article and supplementary information (SI). The raw data are available from the corresponding author upon reasonable request. Supplementary information: sample preparation, experimental methods, calculation methods, results of theoretical calculations, and spectral data. See DOI: https://doi.org/10.1039/d5sc09357k.

Acknowledgements

References

1 Y. Jiang, S. Sun, R. Xu, F. Liu, X. Miao, G. Ran, K. Liu, Y. Yi, W. Zhang and X. Zhu, *Nat. Energy*, 2024, **9**, 975–986.

2 J. Dong, Y. Li, C. Liao, X. Xu, L. Yu, R. Li and Q. Peng, *Energy Environ. Sci.*, 2025, **18**, 4982–4995.

3 C. Li, J. Song, H. Lai, H. Zhang, R. Zhou, J. Xu, H. Huang, L. Liu, J. Gao, Y. Li, M. H. Jee, Z. Zheng, S. Liu, J. Yan, X.-K. Chen, Z. Tang, C. Zhang, H. Y. Woo, F. He, F. Gao, H. Yan and Y. Sun, *Nat. Mater.*, 2025, **24**, 433–443.

4 Y. Zhang, H. Xia, J. Yu, Y. Yang and G. Li, *Adv. Mater.*, 2025, e2504063.

5 F. Furlan and N. Gasparini, *Nat. Mater.*, 2025, **24**, 336–337.

6 Q. Liu and K. Vandewal, *Adv. Mater.*, 2023, **35**, 2302452.

7 J. Wang, H. Yao, Y. Xu, L. Ma and J. Hou, *Mater. Chem. Front.*, 2021, **5**, 709–722.

8 Y. Kong, H. Chen and L. Zuo, *Adv. Funct. Mater.*, 2025, **35**, 2413864.

9 O. V. Mikhnenko, P. W. M. Blom and T. Q. Nguyen, *Energy Environ. Sci.*, 2015, **8**, 1867–1888.

10 D. He, F. Zhao, C. Wang and Y. Lin, *Adv. Funct. Mater.*, 2022, **32**, 2111855.

11 P. Peumans, A. Yakimov and S. R. Forrest, *J. Appl. Phys.*, 2003, **93**, 3693–3723.

12 J. Liu, S. Chen, D. Qian, B. Gautam, G. Yang, J. Zhao, J. Bergqvist, F. Zhang, W. Ma, H. Ade, O. Inganäs, K. Gundogdu, F. Gao and H. Yan, *Nat. Energy*, 2016, **1**, 16089.

13 S. Li, L. Zhan, C. Sun, H. Zhu, G. Zhou, W. Yang, M. Shi, C. Li, J. Hou, Y. Li and H. Chen, *J. Am. Chem. Soc.*, 2019, **141**, 3073–3082.

14 G. Zhou, M. Zhang, Z. Chen, J. Zhang, L. Zhan, S. Li, L. Zhu, Z. Wang, X. Zhu, H. Chen, L. Wang, F. Liu and H. Zhu, *ACS Energy Lett.*, 2021, **6**, 2971–2981.

15 H. Ohkita, S. Cook, Y. Astuti, W. Duffy, S. Tierney, W. Zhang, M. Heeney, I. McCulloch, J. Nelson, D. D. C. Bradley and J. R. Durrant, *J. Am. Chem. Soc.*, 2008, **130**, 3030–3042.

16 S.-i. Natsuda, T. Saito, R. Shirouchi, Y. Sakamoto, T. Takeyama, Y. Tamai and H. Ohkita, *Energy Environ. Sci.*, 2022, **15**, 1545–1555.

17 G. Zhang, X.-K. Chen, J. Xiao, P. C. Y. Chow, M. Ren, G. Kupgan, X. Jiao, C. C. S. Chan, X. Du, R. Xia, Z. Chen, J. Yuan, Y. Zhang, S. Zhang, Y. Liu, Y. Zou, H. Yan, K. S. Wong, V. Coropceanu, N. Li, C. J. Brabec, J.-L. Bredas, H.-L. Yip and Y. Cao, *Nat. Commun.*, 2020, **11**, 3943.

18 T. Zaima, W. Ota, N. Haruta, M. Uejima, H. Ohkita and T. Sato, *J. Phys. Chem. Lett.*, 2023, **14**, 9706–9712.

19 E. Sebastian and M. Hariharan, *ACS Energy Lett.*, 2022, **7**, 696–711.

20 Z. Huang, X. Kang, D. Liu, Y. He, Y. Wu, X. Ding, X. Bao, L. Yu and M. Sun, *Mater. Lett.*, 2022, **315**, 131952.

21 A. Yahagh, R. R. Kaswan, S. Kazemi, P. A. Karr and F. D'Souza, *Chem. Sci.*, 2024, **15**, 906–913.

22 S. Hayakawa, A. Kawasaki, Y. Hong, D. Uraguchi, T. Ooi, D. Kim, T. Akutagawa, N. Fukui and H. Shinokubo, *J. Am. Chem. Soc.*, 2019, **141**, 19807–19816.

23 Z. Liu, G. Zhang, Z. Cai, X. Chen, H. Luo, Y. Li, J. Wang and D. Zhang, *Adv. Mater.*, 2014, **26**, 6965–6977.

24 G. Li, Y. Zhang, T. Liu, S. Wang, D. Li, J. Li, F. Li, L.-M. Yang, Z. Luo, C. Yang, H. Yan, P. Hao, Q. Shang and B. Tang, *J. Mater. Chem. C*, 2018, **6**, 11111–11117.

25 P. E. Hartnett, A. Timalsina, H. S. S. R. Matte, N. Zhou, X. Guo, W. Zhao, A. Facchetti, R. P. H. Chang, M. C. Hersam, M. R. Wasielewski and T. J. Marks, *J. Am. Chem. Soc.*, 2014, **136**, 16345–16356.

26 Y. Wang, H. Zhong, Y. Hong, T. Shan, K. Ding, L. Zhu, F. Liu, H. Wei, C. Yu and H. Zhong, *J. Mater. Chem. C*, 2020, **8**, 8224–8233.

27 W. Zhu, J. M. Alzola, T. J. Aldrich, K. L. Kohlstedt, D. Zheng, P. E. Hartnett, N. D. Eastham, W. Huang, G. Wang, R. M. Young, G. C. Schatz, M. R. Wasielewski, A. Facchetti, F. S. Melkonyan and T. J. Marks, *ACS Energy Lett.*, 2019, **4**, 2695–2702.

28 W. Kim, A. Nowak-Król, Y. Hong, F. Schlosser, F. Würthner and D. Kim, *J. Phys. Chem. Lett.*, 2019, **10**, 1919–1927.

29 E. Sebastian and M. Hariharan, *J. Am. Chem. Soc.*, 2021, **143**, 13769–13781.

30 A. Mazumder, K. Vinod, A. C. Thomas and M. Hariharan, *J. Phys. Chem. Lett.*, 2025, **16**, 4819–4827.

31 Y. Guo, Z. Ma, X. Niu, W. Zhang, M. Tao, Q. Guo, Z. Wang and A. Xia, *J. Am. Chem. Soc.*, 2019, **141**, 12789–12796.

32 C. Lin, T. Kim, J. D. Schultz, R. M. Young and M. R. Wasielewski, *Nat. Chem.*, 2022, **14**, 786–793.

33 T. Kirchartz, G. Yan, Y. Yuan, B. K. Patel, D. Cahen and P. K. Nayak, *Nat. Rev. Mater.*, 2025, **10**, 335–354.

34 H. Wang, M. Li, Y. Liu, J. Song, C. Li and Z. Bo, *J. Mater. Chem. C*, 2019, **7**, 819–825.

35 S. Kang, T. Kim, Y. Hong, F. Würthner and D. Kim, *J. Am. Chem. Soc.*, 2021, **143**, 9825–9833.

36 G. Ran, J. Zeb, Y. Song, P. A. Denis, U. Ghani and W. Zhang, *J. Phys. Chem. C*, 2022, **126**, 3872–3880.

37 M. Son, K. H. Park, C. Shao, F. Würthner and D. Kim, *J. Phys. Chem. Lett.*, 2014, **5**, 3601–3607.

38 F. Würthner, *J. Org. Chem.*, 2022, **87**, 1602–1615.

39 N. J. Hestand and F. C. Spano, *Chem. Rev.*, 2018, **118**, 7069–7163.

40 C. Kaufmann, W. Kim, A. Nowak-Król, Y. Hong, D. Kim and F. Würthner, *J. Am. Chem. Soc.*, 2018, **140**, 4253–4258.

41 J. Kong, W. Zhang, G. Li, D. Huo, Y. Guo, X. Niu, Y. Wan, B. Tang and A. Xia, *J. Phys. Chem. Lett.*, 2020, **11**, 10329–10339.

42 R. Roy, S. Chawla, V. Sharma, A. K. Pal, Y. Silori, A. Datta, A. K. De and A. L. Koner, *Chem. Sci.*, 2024, **15**, 6363–6377.

43 Y. Wang, H. Chen, H. Wu, X. Li and Y. Weng, *J. Am. Chem. Soc.*, 2009, **131**, 30–31.

44 T. Lu, *Molclus*, Version 1.13, http://www.keinsci.com/research/molclus.html.

45 I. Read, A. Napper, R. Kaplan, M. B. Zimmt and D. H. Waldeck, *J. Am. Chem. Soc.*, 1999, **121**, 10976–10986.

46 A. F. Coleman, M. Chen, J. Zhou, J. Y. Shin, Y. Wu, R. M. Young and M. R. Wasielewski, *J. Phys. Chem. C*, 2020, **124**, 10408–10419.

47 T. He, Y. Zhang, H. Zhang, J. Zhao, H. Shi, H. Yang and P. Yang, *ChemSusChem*, 2023, **16**, e202300500.

48 A. J. Gillett, A. Privitera, R. Dilmurat, A. Karki, D. Qian, A. Pershin, G. Londi, W. K. Myers, J. Lee, J. Yuan, S.-J. Ko, M. K. Riede, F. Gao, G. C. Bazan, A. Rao, T.-Q. Nguyen, D. Beljonne and R. H. Friend, *Nature*, 2021, **597**, 666–671.

49 M. Söderberg, B. Dereka, A. Marrocchi, B. Carlotti and E. Vauthey, *J. Phys. Chem. Lett.*, 2019, **10**, 2944–2948.

50 B. Dereka, A. Rosspeintner, Z. Li, R. Liska and E. Vauthey, *J. Am. Chem. Soc.*, 2016, **138**, 4643–4649.

51 B. Dereka, D. Svechkarev, A. Rosspeintner, A. Aster, M. Lunzer, R. Liska, A. M. Mohs and E. Vauthey, *Nat. Commun.*, 2020, **11**, 1925.

52 A. Yamakata, J. J. M. Vequizo and M. Kawaguchi, *J. Phys. Chem. C*, 2015, **119**, 1880–1885.

53 A. Yamakata, K. Kato, T. Urakami, S. Tsujimura, K. Murayama, M. Higashi, H. Sato, Y. Kobori, T. Umeyama and H. Imahori, *Chem. Sci.*, 2024, **15**, 12686–12694.

54 C. E. Ramirez, S. Chen, N. E. Powers-Riggs, I. Schlesinger, R. M. Young and M. R. Wasielewski, *J. Am. Chem. Soc.*, 2020, **142**, 18243–18250.

55 A. Mazumder, K. Vinod, A. Tharamel, P. D. Maret, A. Rajendran and M. Hariharan, *Chem. Commun.*, 2025, **61**, 17641–17644.